

Magnetization-step spectra of $(\text{CH}_3\text{-NH}_3)_2\text{Mn}_x\text{Cd}_{1-x}\text{Cl}_4$ at 20 mK: Fine structure and the second-largest exchange constant

Xavier Gratens, Armando Paduan-Filho, Valdir Bindilatti,* and Nei Fernandes Oliveira, Jr.
Instituto de Física, Universidade de São Paulo, Caixa Postal 66.318, 05315-970 São Paulo-SP, Brazil

Yaacov Shapira[†]

Department of Physics and Astronomy, Tufts University, Medford, Massachusetts 02155, USA

(Received 21 August 2006; revised manuscript received 23 February 2007; published 4 May 2007)

The compounds $(\text{CH}_3\text{-NH}_3)_2\text{Mn}_x\text{Cd}_{1-x}\text{Cl}_4$ are among the better physical realizations of a diluted Heisenberg antiferromagnet on the square lattice. The magnetization of three powder samples, with $x=0.063$, 0.067 , and 0.157 , was measured at temperatures $T \cong 20$ mK in magnetic fields B up to 17 T. Magnetization-step (MST) spectra were obtained with a much higher resolution than in the earlier MST study at $T=0.6$ K. The earlier study uncovered only two spectral lines, near 6.6 and 13 T. These lines were attributed to nearest-neighbor (NN) pairs. The higher-resolution richer spectrum observed at $T \cong 20$ mK is interpreted using a theory which includes two exchange constants: the largest exchange constant, $J^{(1)}$, and the second-largest, $J^{(2)}$. A summary of the relevant results of this theory is given. The main result of the present work is the determination of $J^{(2)}$ by two independent methods. The first method used a series of MSTs that was observed at $T \cong 20$ mK in magnetic fields below 2 T. These MSTs, interpreted as the MSTs from $J^{(2)}$ pairs, gave $J^{(2)}/k_B = -0.227 \pm 0.010$ K. The second method used the fine-structure (FS) splitting of the spectral line near 6.6 T. It gave $J^{(2)}/k_B = -0.208 \pm 0.006$ K. The FS splitting of the spectral line near 13 T is smaller, as expected, and is consistent with the same value of $J^{(2)}$. Attempts to identify the neighbor (in the cation lattice) that is associated with $J^{(2)}$ were unsuccessful. This failure is attributed to previously observed deviations from a random Mn distribution. The field separation between the strongest spectral line in the FS near 13 T and the strongest line near 6.6 T gave $J^{(1)}/k_B = -4.39 \pm 0.05$ K, in excellent agreement with the earlier MST study. Much earlier measurements of the spin-wave dispersion curves in $(\text{CH}_3\text{-NH}_3)_2\text{MnCl}_4$ identified $J^{(1)}$ as the NN exchange constant J_1 . Comments about the theoretical interpretation of the present data are relegated to two appendixes.

DOI: 10.1103/PhysRevB.75.184405

PACS number(s): 75.50.Ee, 71.70.Gm, 75.10.Nr, 75.60.Ej

I. INTRODUCTION

Small clusters of spins occur in strongly diluted magnetic materials and in magnetic molecules. When the intracluster exchange interaction is antiferromagnetic (AF), such clusters give rise to magnetization steps (MSTs) as a function of magnetic field. A wealth of information about magnetic interactions and spin relaxation was gained from studies of these MSTs. The experimental works and the theoretical developments that accompanied them were reviewed recently, e.g., Refs. 1 and 2.

Although two-dimensional (2D) antiferromagnets have been investigated for a long time,^{3,4} very few studies of MSTs in diluted 2D antiferromagnets have been carried out until recently.⁵ The compound $(\text{CH}_3\text{-NH}_3)_2\text{MnCl}_4$ is one of the better physical realizations of a 2D Heisenberg antiferromagnet on the square lattice.^{3,4,6,7} The reasons for the 2D magnetic behavior are related to the crystal structure, a schematic of which is reproduced in Ref. 8. The Mn^{2+} ions are arranged in parallel layers, with interlayer separation of 9.7 Å. Between these layers are Cl anions and $(\text{CH}_3\text{-NH}_3)$ groups. The in-layer nearest-neighbor (NN) Mn^{2+} ions are separated by 5.1 Å. The superexchange bond between these NN's involves a single intervening Cl anion. The exchange interaction between different layers involves exchange paths through both Cl anions and $(\text{CH}_3\text{-NH}_3)$ groups, and it may be reduced further by symmetry.⁶

The Mn^{2+} ion is an S -state ion with spin $S=5/2$. Its single-ion anisotropy is very low, as expected for an

S -state ion. The in-layer NN exchange constant in $(\text{CH}_3\text{-NH}_3)_2\text{MnCl}_4$ is $J_1/k_B \cong -5$ K, where k_B is the Boltzmann constant. All other exchange constants are much smaller. The related series of compounds $(\text{CH}_3\text{-NH}_3)_2\text{Mn}_x\text{Cd}_{1-x}\text{Cl}_4$, in which a large fraction of the Mn^{2+} cations are replaced by Cd^{2+} cations, are expected to be good physical realizations of a strongly diluted Heisenberg antiferromagnet on the square lattice.

The first experimental study⁸ of MSTs from $(\text{CH}_3\text{NH}_3)_2\text{Mn}_x\text{Cd}_{1-x}\text{Cl}_4$ was carried out at temperature $T=0.6$ K, in magnetic fields B up to 17 T. For the range of x that was studied, $0.025 \leq x \leq 0.265$, these compounds do not exhibit long-range magnetic order. The thermal energy $k_B T$ at 0.6 K was small compared to J_1 , but large compared to all other exchange constants. The observed MST spectra were therefore reasonably well explained by a theoretical model⁹ which included only J_1 . The MST data at 0.6 K gave $J_1/k_B = -4.39 \pm 0.10$ K.

The present study at $T \cong 20$ mK was performed on some of the materials that had been studied at 0.6 K. The much lower temperature in the present work increased the resolution of the MST spectra considerably. It was then possible to test some recent predictions for models with two exchange constants.^{10,11}

The small size of the second-largest exchange constant prevented its detection at 0.6 K. In the present work at 20 mK this exchange constant was measured by two methods. One method used the low-field MSTs from pairs with

this exchange constant. The second used line splitting in the high-field fine structure (FS). The results of the two methods are in reasonable (10%) agreement. The previous determination of the largest exchange constant from MSTs at 0.6 K was confirmed by the new data at 20 mK. A neutron-diffraction study of spin waves,⁷ which predated the MST studies, identified this largest exchange constant as the NN exchange constant J_1 .

II. RECENT THEORETICAL MODELS WITH TWO EXCHANGE CONSTANTS

The first theoretical work on MSTs from a diluted antiferromagnet with a square lattice⁹ used the NN cluster model, which only includes the NN exchange constant J_1 . Theoretical works which include both the largest and second-largest exchange constants are much more recent. The detailed accounts of these recent works are very lengthy.^{10,11} To facilitate the reading of the present paper, the most relevant definitions and concepts are summarized here.

A. Classifications of exchange constants

The exchange constants (the J 's) are classified in two different ways. The traditional classification associates each J with a particular neighbor in the cation lattice. The relevant neighbor is specified by a subscript, i.e., J_1 , J_2 , and J_3 are the nearest-neighbor, second-neighbor, and third-neighbor exchange constants, respectively. For the planar (2D) magnetic materials under consideration, only in-plane neighbors are included.

The classification of J 's by neighbors is standard, but it has a practical drawback. Measurements of MSTs often give the magnitude of J without immediately revealing the associated neighbor. It is then convenient to classify the J 's by their relative size. Using superscripts, $J^{(1)}$ is the largest exchange constant, $J^{(2)}$ is the second-largest, etc.

In the present work, both $J^{(1)}$ and $J^{(2)}$ were measured directly. An early neutron-diffraction study,⁷ identified $J^{(1)}$ as the NN exchange constant J_1 . In the two recent theoretical works that are summarized here^{10,11} this identification is assumed. In addition, it is assumed that $J^{(2)}$ is either J_2 or J_3 .

B. Cluster models and cluster types

1. Cluster models

Any cluster model includes only a subset of all possible J 's, classified by neighbors. Reference 9 was devoted to the J_1 model, with the additional assumption that J_1 is $J^{(1)}$. Both Ref. 10 and Ref. 11 were devoted to specific models with two exchange constants: the J_1 - J_2 and J_1 - J_3 models. These are the only models consistent with $J^{(1)}=J_1$, and $J^{(2)}=J_2$ or J_3 . The basic difference between Ref. 10 and Ref. 11 is that in the former the ratio $J^{(2)}/J^{(1)}$ can have any value smaller than 1, whereas in the latter $J^{(2)}/J^{(1)} \leq 1$.

Among the cation sites, only a fraction x is occupied by magnetic ions. The fraction x is called the magnetic-ion "concentration." In theories of MSTs it is assumed that x is well below the site percolation concentration x_c for the rel-

evant cluster model. The values of x_c are 0.407 for the J_1 - J_2 model, and 0.337 for the J_1 - J_3 model.^{12,13} For the J_1 model, $x_c=0.593$.

2. Clusters and their classifications by size and by type

Consider a diluted antiferromagnet, and assume that a specific cluster model, with a specified set of J 's, has already been selected. Each magnetic ion (spin) is then a member of a particular cluster. All the spins in this cluster are coupled to each other by the J 's of the model, but spins in different clusters are not coupled. The cluster size, n_c , is the number of spins in the cluster.

The classification of clusters by size is useful in a variety of problems,¹⁴ but is inadequate for treating MSTs theoretically. The reason is that MSTs are caused by *energy-level crossings* that change the ground states of clusters (see, e.g., Sec. II of Ref. 1). In an increasing magnetic field B , the new ground state of a cluster always has a larger magnetic moment. Changes of ground states of clusters are therefore accompanied by abrupt jumps of the magnetization M , if the temperature T is very low. Crossings of energy levels are governed by the cluster Hamiltonian, not by the cluster size. Therefore, in the theory of MSTs, clusters are classified by their Hamiltonians. The classification by Hamiltonians is the classification by "types."

In the Heisenberg model considered here, the cluster Hamiltonian includes only an isotropic-exchange interaction and an isotropic Zeeman interaction. The Zeeman interaction involves a g -factor, whose value is assumed to be given. The exchange interaction is specified by the complete set of non-zero J 's between the spins of the cluster. This set of J 's can be specified, in turn, by a "bond list." Bond lists, in which the J 's are classified by the associated neighbors, were discussed in detail in Ref. 9.

A bond list, together with value of g , specify the cluster Hamiltonian. The classification of clusters by bond lists is the classification by types. In addition to specifying the cluster type the bond list also gives, indirectly, the cluster size n_c . Although it is redundant, it is usual to state the cluster size n_c in addition to giving the bond list.

3. Multiple cluster types for the same cluster size

For either the J_1 - J_2 model or the J_1 - J_3 model on the square lattice, there is more than one cluster type for any cluster size n_c . The only exception is the smallest size, $n_c=1$, which corresponds to an isolated spin (called a "single"). For $n_c=2$, there are already two cluster types: a J_1 pair and a J_2 pair in the J_1 - J_2 model, or a J_1 pair and a J_3 pair in the J_1 - J_3 model. For both models, all cluster types and their bond lists were given for each cluster size up to $n_c=5$ (Ref. 10). These results were later extended by Bindilatti to cluster sizes up to $n_c=8$ (Ref. 15).

The number of cluster types for a given size n_c increases rapidly with n_c . In the J_1 - J_2 model on the square lattice there are 4, 15, 45, 186, 759, and 3486 cluster types for $n_c=3, 4, 5, 6, 7$, and 8, respectively. For the J_1 - J_3 model the corresponding numbers are 4, 17, 58, 284, 1409, and 7883 cluster types.

4. Statistics of cluster types

The statistics of each of these numerous cluster types was discussed in Refs. 10 and 15. The probabilities that a randomly chosen spin is in a cluster of each of these types were obtained. They were expressed analytically as a function of the magnetic-ion concentration x . The central assumption was a random distribution of the magnetic ions over the cation sites. Cluster probabilities do not depend on the spin S of the magnetic ions.

C. MST spectrum

Except for the “single” (isolated spin), each cluster type gives rise to abrupt jumps (MSTs) in the low-temperature magnetization curve, M versus B . In the derivative curve, dM/dB versus B , each MST appears as a sharp peak. The pattern of peaks in the derivative curve is called the MST spectrum. A single peak is a “spectral line.” The full spectrum is the superposition of the spectra from all the cluster types. Plots of MST spectra are very effective for visual presentations of experimental and theoretical results on MSTs.

D. Truncation at a maximum cluster size

All cluster types contribute to the magnetization $M(T, B)$. The full theoretical expression for M is an infinite sum of contributions from all cluster types. Each contribution depends on the energy levels and on the probability for the cluster type.

The energy levels and probabilities are calculated only for a finite number of cluster types. The infinite sum that gives M exactly is therefore truncated. The “truncated sum” includes the exact contributions from only a finite number of cluster types. The “remainder” contains the contributions from all other cluster types.

Typically, the truncated sum includes all cluster types with sizes no larger than a maximum size, called n_{max} . The remainder contains the contributions from clusters with $n_c > n_{\text{max}}$. The magnetization M and MST spectrum are calculated only from the truncated sum. The spectrum from the remainder cannot be recovered after the truncation. In some cases, however, it is still possible to *approximate* the contribution of the remainder to M , and then add it to the magnetization from the truncated sum.

In the present work the theoretical interpretation of the experimental results is based on the choice $n_{\text{max}}=5$. The motivation for this choice, the values of x for which it can be justified, and the limitations for the other values of x , are discussed in Appendix A. The “corrective quintets method,” described in Ref. 11, is a method of approximating the magnetization from the remainder when $n_{\text{max}}=5$.

E. Working model

The working model is the actual model that is used for calculating the spectrum. It involves the following choices. First and foremost are the choices of the cluster model (J_1 - J_2 or J_1 - J_3) and of the cutoff cluster size n_{max} . These choices determine the cluster types that are included in the working model. Then there are some specific parameters: the

magnetic-ion concentration x , the spin S , the g -factor, and the numerical values of the two exchange constants.

F. Lopsided models

1. Definition and criterion for a lopsided working model

When the two AF exchange constants in the working model are comparable in size, the calculated MST spectrum is quite complicated. The spectrum is much simpler if one of the J 's is much smaller than the other. The term “lopsided model” is used when there is a “sufficiently large” disparity between the magnitudes of the two J 's in the working model. The defining feature of a lopsided working model is the existence of a gap in the calculated spectrum. The gap is a magnetic field range in which there are no spectral lines. The calculated spectrum then has two separate parts: a low-field part (below the gap), and a high-field part (above the gap).

Lopsided models were discussed in Ref. 11. The criterion that a working model is lopsided was stated as the maximum ratio between the smaller and the larger J 's for which a gap still exists. This maximum ratio depends on two parameters of the working model: the spin S , and the maximum cluster size n_{max} . The maximum ratio of the J 's was obtained for $S=5/2$ when $n_{\text{max}}=2, 3, 4$, or 5. For all these values the criterion for being lopsided is the same for working models based on the J_1 - J_2 and on the J_1 - J_3 cluster models. That is, the maximum ratios $(J_2/J_1)_{\text{max}}$ and $(J_3/J_1)_{\text{max}}$ for which a gap still exists are the same.

2. Relating the MST spectrum of a lopsided model to the exchange-bond structure

The interpretation of the calculated MST spectrum is simplified considerably if it is known that the working model is lopsided. Only a finite number of cluster types are included in the working model. When the model is lopsided, the spectrum from each of these cluster types can be related directly to the exchange-bond structure specified by the bond list for this cluster type.

A lopsided working model has two widely different energy scales, determined by the strong and the weak exchange constants. All spectral lines below the gap originate from abrupt changes in the exchange energy associated with weak exchange bonds, i.e., J_2 or J_3 bonds. Abrupt changes in the energy associated with strong exchange bonds (J_1 bonds) occur only at spectral lines above the gap.

The integrated intensities of spectral lines are proportional to the sizes of the associated jumps in M . Below the gap the most intense spectral lines arise from pairs, each consisting of two spins coupled by the weak exchange bond. Depending on the cluster model these are J_2 pairs or J_3 pairs. The magnetic-field separations between these most intense lines in the low-field part of the spectrum can be used to determine the *magnitude* of the weak exchange constant. It is more difficult to identify this J as J_2 or J_3 .

Any spectral line above the gap involves an abrupt change in the energy associated with strong exchange bonds. There may also be a simultaneous abrupt change in the energy associated with the weak exchange bonds. The magnetic field

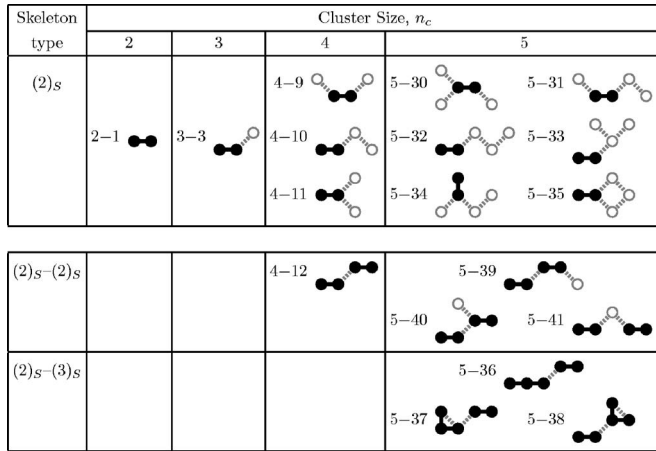


FIG. 1. Skeletons and decorations in 18 of the cluster types of the J_1 - J_2 cluster model. Solid and empty circles correspond to skeleton spins and decoration spins, respectively. Solid and dashed lines correspond to J_1 bonds and J_2 bonds, respectively. The upper part of the figure is for 11 of these cluster types in which the skeleton is simple. The lower part is for the seven cluster types with a compound skeleton.

of any line above the gap is determined primarily by the strong bonds. The weak exchange bonds can shift the field of a high-field line only slightly.

G. Skeletons and decorations

The high-field lines from a particular cluster type are related directly to its exchange-bond structure, which must include at least one strong exchange bond. The concepts of “skeletons” and “decorations” are central for exposing these relations. The discussion below is for a lopsided working model based on the J_1 - J_2 cluster model. A completely analogous discussion applies when the working model is based on the J_1 - J_3 model.

1. Definitions

Any cluster type that produces spectral lines above the gap has at least one J_1 bond (strong bond). Each individual cluster of this type has a skeleton. The skeleton consists of all the J_1 bonds of the cluster together with all the spins that are attached to these bonds. No weak exchange bond (J_2 bond) is ever included in the skeleton, even if this J_2 bond is attached to a skeleton spin.

The “decoration” of the cluster consists of all the spins and all the exchange bonds in the cluster that are not included in the skeleton. Any exchange bond in a decoration must be a weak bond (J_2 bond). If all the spins of a cluster are already in the skeleton, the decoration consists only of J_2 bonds between skeleton spins. If there are no J_2 bonds, a decoration does not exist or, alternatively, the cluster has a “null decoration.”

Figure 1 shows the skeletons and decorations in 18 of the cluster types of the J_1 - J_2 model. The skeletons are emphasized by representing skeleton spins as solid circles, and J_1 bonds as solid lines. Decoration spins are shown as empty

circles, and J_2 bonds as dashed lines. Cluster type 2-1 has a null decoration.

2. Simple skeletons and their types

A skeleton with the property that any two of its spins are connected by at least one continuous path of J_1 bonds is called a “simple” skeleton. Examples are the 11 skeletons in the upper part of Fig. 1, each of which consists of two spins connected by a J_1 bond. Any of these 11 simple skeletons is identical to a J_1 pair, which is cluster type 2 in the J_1 model (see Fig. 3 of Ref. 9). These 11 skeletons are classified as type $(2)_S$, where the subscript “S” indicates that it is a skeleton type and not a cluster type.

Other simple skeletons (not shown) are identical to other cluster types of the J_1 model. For example, one type of a simple skeleton is identical to cluster type 3 of the J_1 model, which is a J_1 triplet. This simple skeleton is therefore classified as type $(3)_S$.

3. Compound skeletons and their classification

Examples of “compound skeletons” are shown in the lower part of Fig. 1. Each of these seven compound skeleton consists of two “fragments.” All spins in each fragment are connected by at least one continuous path of J_1 bonds. The two fragments are connected by a J_2 bond, except for cluster type 5-41 in which the fragments are bridged by two consecutive J_2 bonds and a decoration spin.

Fragments are classified by types, in analogy to the classification of simple skeletons by types. All fragments in the lower part of Fig. 1 are either of type $(2)_S$ or of type $(3)_S$, i.e., a J_1 pair or a J_1 triplet. A compound skeleton as a whole is classified by giving all its fragment types. In Fig. 1 the compound skeletons in cluster types 4-12, 5-39, 5-40, and 5-41 are of type $(2)_S-(2)_S$. Those in cluster types 5-36, 5-37, and 5-38 are of type $(2)_S-(3)_S$, which is the same as type $(3)_S-(2)_S$.

The concept of a compound skeleton can be generalized to include skeletons with more than two fragments.¹¹ For $n_{\max}=5$, no compound skeleton can have more than two fragments, and no fragment can contain more than three spins. Thus, for example, a fragment of type $(4A)_S$ cannot exist when $n_{\max}=5$, although there are simple skeletons of type $(4A)_S$.

H. Monoskeleton fine structure

The classification of skeletons reveals the main cause of the fine structure in the high-field part of the spectrum. Any FS consists of a group of spectral lines that are very close to each other. The 11 simple skeletons in Fig. 1 are of type $(2)_S$, and the seven compound skeletons in the same figure contain a fragment of type $(2)_S$. The high-field spectral lines produced by these 18 cluster types are shown in Fig. 2. These results are for $S=5/2$. Each of the 18 cluster types produces spectral lines very close to $b_1=2, 4, 6, 8, 10$, where

$$b_1 = g\mu_B B / |J_1| \quad (1)$$

is the “primary reduced magnetic field.”

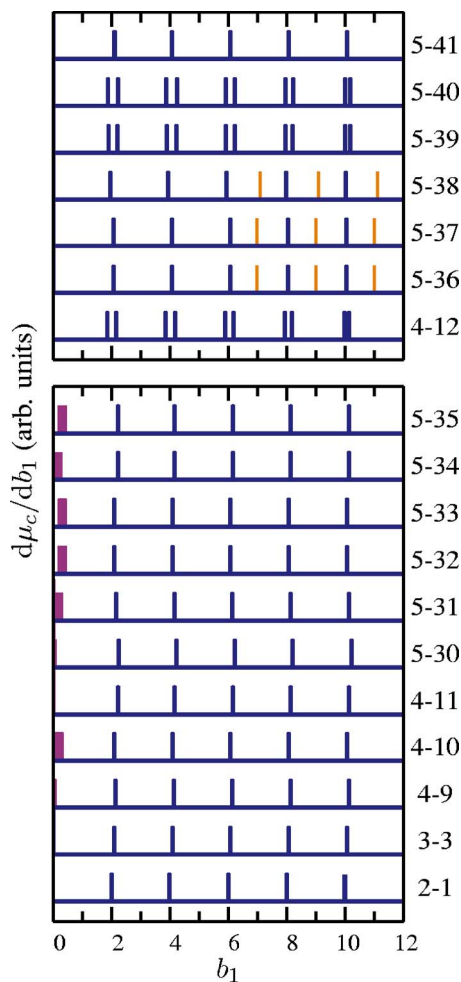


FIG. 2. (Color online) The spectra of all cluster types of the J_1 - J_2 model that contribute to the $(2)_S$ monoskeleton FS when $n_{\max}=5$. Spectral lines in the $(2)_S$ monoskeleton FS are darker (dark blue). The lower part of the figure shows the spectra from cluster types with a simple skeleton of type $(2)_S$. The upper part of the figure shows the spectra from cluster types with a compound skeleton containing a fragment of type $(2)_S$. The labels for the cluster types follow Fig. 1. The abscissa is the primary reduced magnetic field $b_1 = g\mu_B B/|J_1|$. All line intensities are chosen to be equal. These results are for $S=5/2$, $J_2/J_1=0.028$, and $T=0$.

The superposition of the spectra from these 18 cluster types would lead to groups of very close spectral lines near each of these five values of b_1 . These groups of very close lines constitute the $(2)_S$ monoskeleton FS. The FS arises from different decorations that are attached to a $(2)_S$ skeleton or fragment.

For any group of close lines in a monoskeleton FS, the magnetic-field separations are of order $b_2 \sim 1$, where

$$b_2 = g\mu_B B/|J_2| \quad (2)$$

is the “secondary reduced magnetic field.”

In addition to the lines near $b_1=2, 4, \dots, 10$, Fig. 2 also shows some lines near $b_1=7, 9$, and 11. These additional lines are part of the $(3)_S$ monoskeleton FS. They originate from the $(3)_S$ fragment in the $(2)_S$ - $(3)_S$ compound skeletons

of cluster types 5-36, 5-37, and 5-38. A fragment of type $(3)_S$ is identical to a cluster of type 3 in the J_1 model (Fig. 3 of Ref. 9), which is a “pure” J_1 triplet.

I. High intensity lines in the high-field part of the MST spectrum

The intensities of the spectral lines are governed by cluster statistics. Above the gap the most intense spectral lines, at least for $x < 0.2$, are from pure J_1 pairs. These pairs correspond to cluster type 2-1 in both the J_1 - J_2 and the J_1 - J_3 models. For $S=5/2$, the 2-1 lines are exactly at $b_1=2n$, where $n=1, 2, \dots, 5$. Slightly above each of these fields there is a line from cluster type 3-3, which corresponds to a J_1 pair that is connected to a third spin by a weak exchange bond (Fig. 1). The 3-3 lines have the second-highest intensity above the gap. Both the 2-1 lines and the 3-3 lines belong to the $(2)_S$ monoskeleton FS (see Fig. 2).

The spectrum above the gap includes five conspicuous asymmetric doublets, each consisting of a strong 2-1 line (at $b_1=2n$, where $n=1, 2, \dots, 5$) followed by a weaker 3-3 line. The field splitting within each of the doublets, which depends on n , was first calculated by Vu.^{1,11,16} Using these results, the observed splitting in any of these conspicuous doublets can be used to determine the smaller exchange constant. Identifying this exchange constant as J_2 or J_3 is much more difficult.

III. EXPERIMENTAL TECHNIQUES

A. Samples

Crystals of $(\text{CH}_3\text{-NH}_3)_2\text{Mn}_x\text{Cd}_{1-x}\text{Cl}_4$ were grown from solution, as described earlier.⁸ Three powder samples, called “B,” “C,” and “E,” were used in the present work. They were portions of “products” B, C, and E of Ref. 8, respectively. The Mn concentrations x for these products, taken from the last column of Table I in Ref. 8, are $x=0.063 \pm 0.011$ for B, $x=0.067 \pm 0.008$ for C, and $x=0.157 \pm 0.008$ for E. These are the best available values of x for the samples used in the present work.

B. Magnetization measurements

The magnetization M was measured at $T \approx 20$ mK. Two plastic dilution refrigerators were used.¹⁷ Sample “B” was measured at 24 mK in one refrigerator. Samples “C” and “E” were measured at 16 mK in the other refrigerator. The main magnetic field B was generated by a Nb_3Sn superconducting magnet, with a maximum field of 17 T. The field sweep rate, $|dB/dt|$, was 0.17 T/min for sample “B,” and 0.43 T/min for both samples “C” and “E.”

The magnetization was measured by the force method. The experimental setup and procedures were similar to those described earlier.¹⁷ The magnetic force acting on the sample was produced by a magnetic-field gradient, generated by a superconducting gradient coil. This gradient was superimposed on the main magnetic field from the Nb_3Sn magnet. A typical gradient of about 10 T/m (equivalent to 1 kG/cm), and a typical sample length of 3 mm, resulted in a field

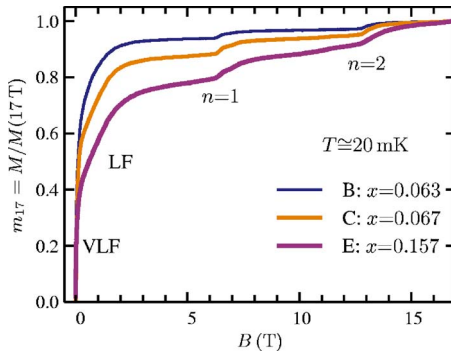


FIG. 3. (Color online) Magnetization curves of the three samples over the full range of the magnetic field B . The ordinate m_{17} is the magnetization M normalized to its value at 17 T. The very-low-field region, the low-field region, and the field regions $n=1$ and $n=2$, are indicated.

variation $(\delta B)_{\text{grad}} \cong 0.03$ T over the sample. The currents in the superconducting gradient coil and in the Nb_3Sn magnet were controlled independently.

The magnetic force was measured by a capacitance technique. The output signal included a small spurious background. This background was determined by repeating the measurement with no current in the gradient coil. The background was then subtracted from the total output signal.

IV. RESULTS

A. Magnetization curves for the full field range

The isothermal magnetization M was measured as a function of B at $T \cong 20$ mK. For each sample, two sets of data in increasing B and two in decreasing B were taken over the full field range. Additional data over limited field ranges were taken for sample “B.” The results showed practically no hysteresis.

Figure 3 shows the magnetization curves for the full field range. Each curve is an average of the data for increasing and decreasing B . The ordinate $m_{17} = M(B)/M(17 \text{ T})$ is the magnetization normalized to its value at the highest available field, 17 T. In the theoretical papers M was normalized to its saturation value M_0 , which is a different normalization.

The curves in Fig. 3 exhibit the following gross features in increasing B :

(1) In the very-low-field (VLF) region, B below a small fraction of 1 T, the magnetization M rises very rapidly, due to the alignment of the magnetic moments of the singles, and of “spontaneous magnetic moments” of some other cluster types. (Spontaneous magnetic moments are finite magnetic moments in zero magnetic field.)

(2) In the low-field (LF) region, above a small fraction of a tesla but below about 2 T, the magnetization still rises at a moderately fast rate. The rise of M in the LF region is the result of a superposition of MSTs which are related to abrupt changes in the energies of the weak exchange bond. These bonds are those with the smaller exchange constant, $J^{(2)}$.

(3) Two prominent MSTs occur at much higher fields, near 6.6 and 13 T. Each of these MSTs is preceded by a

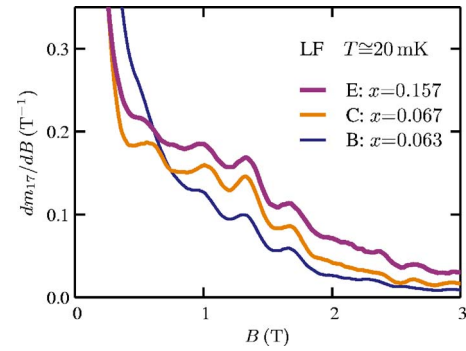


FIG. 4. (Color online) Experimental derivative dm_{17}/dB of the normalized magnetization $m_{17} = M/M(17 \text{ T})$ in the low-field region.

“plateau,” in which the variation of M with B is very slow. The prominent MSTs near 6.6 and 13 T were observed earlier at 0.6 K, but with a much lower resolution.⁸ They were interpreted as the first ($n=1$) and the second ($n=2$) MSTs from NN pairs, respectively. This interpretation was based on the J_1 model. The present study demonstrates that at $T \cong 20$ mK these MSTs develop a fine structure. Such a FS is expected from a model which includes both J_1 and $J^{(2)}$ when $J^{(2)}$ is much smaller than J_1 .¹¹ In Fig. 3 the field regions near 6.6 and 13 T are labeled as $n=1$ and $n=2$, even though the FS’s in these field regions include spectral lines other than the $n=1$ and $n=2$ lines from pure NN pairs.¹⁸

B. Derivative curves in the low-field region

1. MSTs in the LF region

The structure of the magnetization curves in the LF region of Fig. 3 is revealed by the derivative curves, dm_{17}/dB versus B . These curves, which were obtained by numerical differentiation, are shown in Fig. 4. Samples “C” ($x=0.067$) and “E” ($x=0.157$) exhibit four peaks below 2 T. The last three of these four peaks are also obvious in the curve for sample “B” ($x=0.063$), but for this sample the first of the four peaks barely manifests itself as an inflection point.

From the theory outlined in Sec. II, the most prominent MSTs in the LF region arise from $J^{(2)}$ pairs. Each such pair consists of two spins coupled by a $J^{(2)}$ bond. The four derivative peaks in Fig. 4 are therefore attributed to such pairs. Actually, the $J^{(2)}$ pairs should produce a total of five lines. The first of these lines is not seen in Fig. 4 because it occurs in the VLF region. In that field region the line is masked by the large derivative from the singles and the spontaneous magnetic moments.

2. Linewidths

The derivative peaks in Fig. 4 are substantially wider than expected from thermal broadening alone. The theoretical thermal width $(\delta B)_T$ is given by¹

$$(\delta B)_T = 3.53k_B T / g\mu_B, \quad (3)$$

where $g=2.0045$ is the g -factor of the Mn^{2+} ion in the present compounds.¹⁹ At 20 mK, the thermal width is only 0.05 T, which is obviously much smaller than the experi-

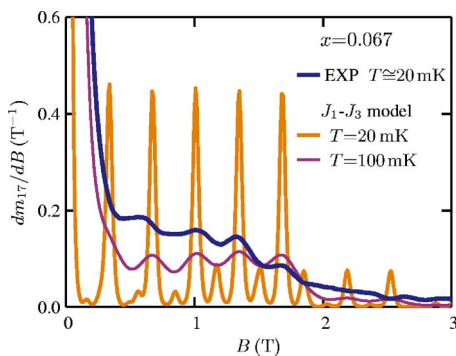


FIG. 5. (Color online) Experimental derivative (EXP) dm_{17}/dB for $x=0.067$ and simulations based on the J_1 - J_3 model (see Ref. 20). One simulation is for the actual experimental temperature, $T=20$ mK. The other is for an effective temperature $T=100$ mK. The simulations use the exchange constants $J_1/k_B=J^{(1)}/k_B=-4.39$ K, and $J_3/k_B=J^{(2)}/k_B=-0.227$ K. These results are for the LF region.

mental linewidths in Fig. 4. To account for the observed linewidths on the basis of thermal broadening alone, it is necessary to assume an effective temperature of about 100 mK.

These conclusions are illustrated in Fig. 5 which shows the derivative of the experimental magnetization curve for $x=0.067$ (sample “C”), and simulations for $T=20$ mK and for $T=100$ mK. Only thermal broadening is included in these simulations.²⁰ The tallest peaks in the simulation for 20 mK are from $J^{(2)}$ pairs. The peaks that are about a factor of 6 smaller are from $J^{(2)}$ triplets.

There are several known *nonthermal* mechanisms of line broadening. Those that are quantifiable include (1) the field variation over the sample, $(\delta B)_{\text{grad}} \cong 0.03$ T, due to the field gradient, and (2) the finite field interval, $(\delta B)_{\text{der}} \cong 0.1$ T, used in the numerical derivative. Mechanisms of line broadening that are not readily quantified include: exchange constants smaller than $J^{(2)}$, weak anisotropies, and local strains.¹

The assumption of unstrained square Mn layers is an idealization. This idealization was used successfully in previous studies of the magnetic properties of these materials, namely, the susceptibility⁶ and the spin-wave dispersion curves.⁷ However, linewidths of MSTs are likely to be more sensitive to strains than these previously studied properties.

The compounds $(\text{CH}_3\text{-NH}_3)_2\text{Mn}_x\text{Cd}_{1-x}\text{Cl}_4$ are among the better physical realizations of the diluted Heisenberg antiferromagnet on the square lattice, but they are not ideal. Crystallographic phase transitions that occur as the samples are cooled (Sec. I of Ref. 8) lead to deviations from square symmetry. Although relatively small, these deviations are likely to result in strains. Small deviations from square symmetry may also cause some lines of the MST spectrum to split. Although no clear evidence for such line splitting was observed in the data, it is possible that unresolved splitting increased some linewidths.

3. Exchange constant $J^{(2)}$ from the MSTs in the LF region

The second-largest exchange constant $J^{(2)}$ was determined from the field separation $(B_{n+1}-B_n)$ between successive MSTs from $J^{(2)}$ pairs. The relevant equation is^{1,10}

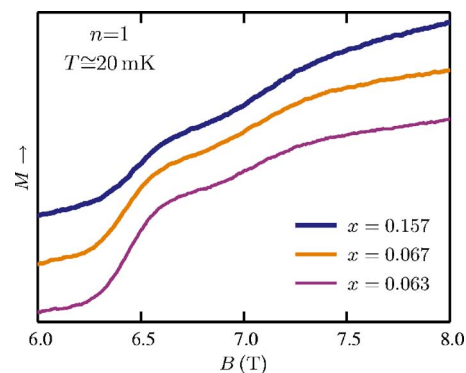


FIG. 6. (Color online) Magnetization curves in the field region $n=1$. The vertical gains for the three curves were adjusted so that between 6.0 and 8.0 T the change of the ordinate is the same for all samples.

$$g\mu_B(B_{n+1}-B_n) = 2|J^{(2)}|. \quad (4)$$

Analysis of the derivative curves in Fig. 4, and of similar derivative curves obtained with somewhat smaller $(\delta B)_{\text{der}}$, led to the following average separations between successive MSTs: 0.336 T for sample “B” ($x=0.063$), 0.337 T for sample “C” ($x=0.067$), and 0.338 T for sample “E” ($x=0.157$). The spread in these values is much smaller than a realistic estimate of the actual uncertainty. The overall average separation and its estimated uncertainty are $(B_{n+1}-B_n) = 0.337 \pm 0.015$ T. Equation (4) then gives $J^{(2)}/k_B = -0.227 \pm 0.010$ K.

C. Fine structure near the first MST from NN pairs

The field region $n=1$ (Fig. 3) is near the first MST from “pure” J_1 pairs.¹⁸ The magnetization curves at $T \cong 20$ mK for this field region are shown in Fig. 6. The vertical gains for these curves were adjusted so that between 6.0 and 8.0 T the change in the ordinate is the same for all three samples.

Each curve in Fig. 6 exhibits two well-resolved successive rises of M with increasing B . The earlier lower-resolution data at 0.6 K (Ref. 8) showed only one rise of M with increasing B in this field range. Thus, what in the earlier work appeared as one MST from NN pairs (J_1 pairs) is actually a superposition of at least two MSTs. The two distinct MSTs in Fig. 6 correspond to a resolved fine-structure (FS) splitting of the single MST observed earlier at 0.6 K.

Details of the FS in the field region $n=1$ are revealed more clearly by the derivative curves in Fig. 7. These rather smooth curves for dM/dB were obtained with $(\delta B)_{\text{der}} \cong 0.16$ T. Derivative curves obtained with smaller $(\delta B)_{\text{der}}$ were noisier, but some were still acceptable for further analysis. Each of the derivative curves in Fig. 7 exhibits two clearly resolved peaks which overlap slightly. Obviously, these two peaks correspond to the two successive magnetization rises in Fig. 6.

The FS in the field region $n=1$ was discussed in Ref. 11. The main result was restated in Sec. II of the present paper. Assuming that $J^{(2)}$ is much smaller than $J^{(1)}=J_1$, and that $J^{(2)}$ is either J_2 or J_3 , two spectral lines in the field region $n=1$

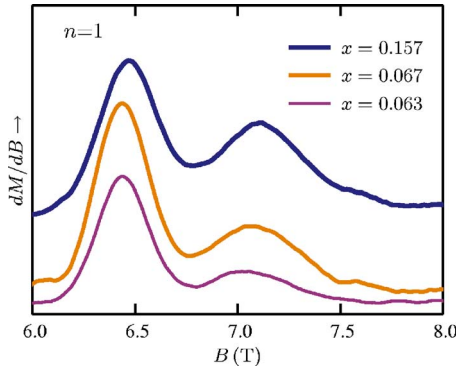


FIG. 7. (Color online) Derivatives of the magnetization curves in Fig. 6, for the field region $n=1$.

have much higher “intensities” than all the others. The strongest line is from pure J_1 pairs (cluster type 2-1). The magnetic field at this line will be called B_1 . The second-strongest line is from “mixed” triplets (cluster type 3-3), each consisting of a J_1 pair attached to a third spin by a $J^{(2)}$ bond. [The triplet is called mixed because it has one J_1 bond and one $J^{(2)}$ bond.] The line from these triplets is at a field B'_1 , which is slightly higher than B_1 .

Each derivative curve in Fig. 7 was interpreted as the superposition of the most intense and the second most intense lines predicted by the theory. The other, much weaker, predicted lines in the field region $n=1$ were ignored. Each curve in Fig. 7 was therefore decomposed into two slightly overlapping peaks. As predicted, the taller peak is at a lower magnetic field. The field at the taller peak was taken as B_1 , and the field at the smaller peak was taken as B'_1 . Alternative methods of decomposing each derivative curve into two peaks gave nearly the same values for B_1 and B'_1 . The results for these magnetic fields are given in Table I. The accuracy of the results for B_1 and B'_1 is expected to be higher for $x=0.063$ and 0.067 than for $x=0.157$. The reason is that the neglect of lines other than those from the cluster types 2-1 and 3-3 is more justified for low x . However, even for $x=0.157$ the results are expected to be quite accurate.

D. Fine structure near the second MST from NN pairs

The field region $n=2$ (Fig. 3) is near the second MST from pure J_1 pairs. The magnetization curves at $T \cong 20$ mK in the field interval from 10 to 15 T are shown in Fig. 8. This field interval is actually slightly wider than the $n=2$ region. The vertical gains for the curves in Fig. 8 were adjusted so

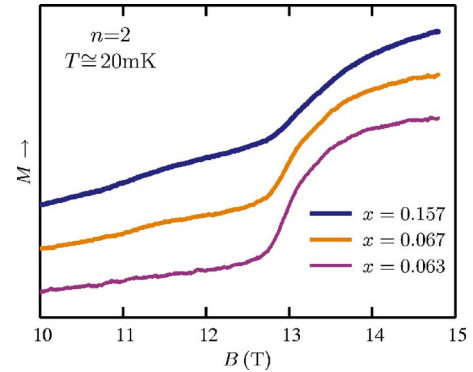


FIG. 8. (Color online) Magnetization curves between 10 and 15 T. This field interval includes the field region $n=2$. The vertical gains were adjusted so that the change in the ordinate between 10 and 15 T is the same for all three curves.

that the change in the ordinate between 10 and 15 T is the same for all three curves. The derivative curves corresponding to Fig. 8 are shown in Fig. 9.

For $B \geq 12$ T the derivative curves in Fig. 9 are qualitatively similar to those in Fig. 7 (field region $n=1$). The main difference is that the separation between the two overlapping peaks is smaller. That is, the overlap is stronger in Fig. 9. The resolution of the two individual overlapping peaks is therefore poorer. As in Fig. 7 the taller of the two overlapping peaks is attributed to pure J_1 pairs, and the smaller to mixed J_1 - $J^{(2)}$ triplets. The magnetic fields at these two peaks are called B_2 and B'_2 , respectively. The values of B_2 , and estimated values of $(B'_2 - B_2)$, are given in Table I. As expected from the theory (Fig. 12 of Ref. 11) the difference $(B'_2 - B_2)$ in the field region $n=2$ is smaller than the difference $(B'_1 - B_1)$ in the region $n=1$.

In Fig. 9, the curve for $x=0.157$ has a broad peak near 11 T, in addition to the larger two overlapping peaks near 13 T. The peak near 11 T is interpreted as a superposition of spectral lines from the so-called $(4A)_S$ monoskeleton FS. In the J_1 model the $4A$ quartets give rise to several MSTs. From Table II of Ref. 9, the third $4A$ spectral line is at $B = (3.389/4.000)B_2 = 0.847B_2$, where B_2 is the field at the second line from pure J_1 pairs. In the present case, $B = 13.0$ T so that the third $4A$ spectral line is near 11.0 T.

When the J_1 model is replaced by the J_1 - $J^{(2)}$ model, with $J^{(2)}/J_1 \ll 1$, each $4A$ line gives rise to a $(4A)_S$ monoskeleton FS (see Fig. 7 of Ref. 11). The FS from the third $4A$ line consists of several close $(4A)_S$ lines near 11 T. The spectral lines near 13 T have a completely different origin. These

TABLE I. Magnetic fields B_1 and B_2 at the tallest peaks in Figs. 7 and 9, respectively. These peaks are attributed to the first and second MSTs from pure J_1 pairs. Also given is the separation $(B'_1 - B_1)$ between the two overlapping peaks in Fig. 7, and the estimated separation $(B'_2 - B_2)$ between the two overlapping peaks in Fig. 9. The peaks at B'_1 and B'_2 are attributed to mixed J_1 - $J^{(2)}$ triplets.

Sample (x)	B_1 (T)	B_2 (T)	$B_2 - B_1$ (T)	$B'_1 - B_1$ (T)	$B'_2 - B_2$ (T)
B (0.063)	6.44	12.95	6.51	0.595	0.42
C (0.067)	6.44	12.95	6.52	0.625	0.45
E (0.157)	6.46	13.00	6.54	0.640	0.44
Average	6.45	12.97	6.52	0.620	0.44

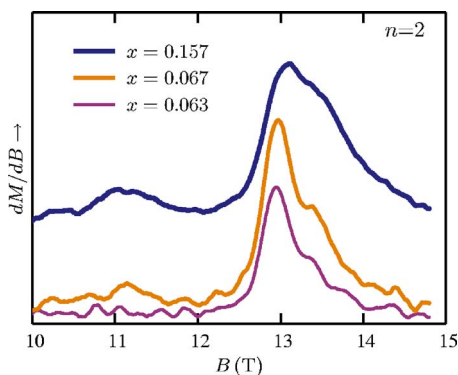


FIG. 9. (Color online) Derivatives of the magnetization curves in Fig. 8, which includes the field region $n=2$.

lines evolve largely from the second line ($n=2$) of the NN pairs in the J_1 model, not from the third line of the 4A quartets of that model.

The $(4A)_S$ monoskeleton lines near 11 T are all from quartets or larger clusters.¹¹ In contrast, the dominant two lines of the FS near 13 T are from pairs and from mixed triplets. The dependence of the statistics of cluster types on cluster size implies that in the range $0.06 \leq x \leq 0.16$ the intensities of the lines near 11 T should grow faster with x than those of the lines near 13 T. For this reason the broad peak near 11 T, in Fig. 9, stands out much more clearly when $x=0.157$ than when $x \cong 0.06$. Small deviations from a random Mn distribution should not invalidate this explanation.

E. Exchange constants from high-field spectral lines

Works on the (undiluted) antiferromagnet $(\text{CH}_3\text{-NH}_3)_2\text{MnCl}_4$ have established that the in-plane NN exchange constant J_1 is the largest exchange constant $J^{(1)}$, and that its magnitude is $J_1/k_B \cong -5$ K.^{6,7} The earlier 0.6 K data on MSTs from $(\text{CH}_3\text{-NH}_3)_2\text{Mn}_x\text{Cd}_{1-x}\text{Cl}_4$ gave $J_1/k_B = -4.39 \pm 0.10$ K.⁸ Prior to the present work the only information about the second-largest exchange constant $J^{(2)}$ was that it is much smaller than $J^{(1)}$. The determination of $J^{(2)}$ from the low-field MSTs due to $J^{(2)}$ pairs was already described in Sec. IV B 3. In what follows, both $J^{(1)}=J_1$ and $J^{(2)}$ are obtained from the high-field results in Table I.

1. Largest exchange constant

The value of $J^{(1)}=J_1$ was determined from the fields B_1 and B_2 of the first and second spectral lines from pure J_1 pairs.¹⁸ The equation⁸⁻¹⁰

$$g\mu_B(B_2 - B_1) = 2|J_1| \quad (5)$$

was used. The average of $(B_2 - B_1)$ in Table I is 6.52 T. The uncertainty, 0.07 T, is largely due to the uncertainty in the calibration of the Nb₃Sn magnet. Taking $g=2.0045$ from Ref. 19, Eq. (5) then gives $J_1/k_B = -4.39 \pm 0.05$ K. This result is in excellent agreement with the value obtained earlier from the MST data at 0.6 K.

2. Second-largest exchange constant

The second-largest exchange constant $J^{(2)}$ was determined from the separation $(B'_1 - B_1)$ between the lines from mixed

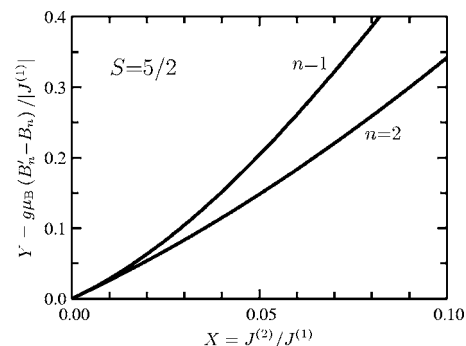


FIG. 10. Calculated difference $Y = g\mu_B(B'_n - B_n)/|J^{(1)}|$ between the primary reduced fields at the mixed-triplet line and at the pure-pair line, plotted as a function of $X = J^{(2)}/J^{(1)}$. The two curves are for the field regions $n=1$ and $n=2$.

triplets and from pure J_1 pairs, in the field region $n=1$. The procedure was outlined in Sec. VI B of Ref. 11. It makes use of the theoretical results in Fig. 12 of that reference.

Figure 10 of the present paper shows a subset of the theoretical results in Fig. 12 of Ref. 11, but using a very different format. The abscissa X in Fig. 10 is the ratio $J^{(2)}/J^{(1)}$, plotted on a linear scale that extends only up to 0.10. The ordinate Y is the normalized field separation $(B'_n - B_n)$ for either of the field regions $n=1$ or $n=2$. Unlike Fig. 12 of Ref. 11, the normalization is based on $J^{(1)}$. That is,

$$Y = g\mu_B(B'_n - B_n)/|J^{(1)}|, \quad (6)$$

where n is either 1 or 2. In the terminology of Sec. II, Y is the separation between the “primary reduced fields” at the line from the mixed J_1 - $J^{(2)}$ triplets and at the line from the pure J_1 pairs. Using Eq. (5) and $J_1=J^{(1)}$, the ordinate Y can also be expressed as

$$Y = 2(B'_n - B_n)/(B_2 - B_1). \quad (7)$$

The curves $n=1$ and $n=2$ in Fig. 10 are for the field regions $n=1, 2$, respectively.

The determination of $J^{(2)}$ used the curve $n=1$ in Fig. 10. In Table I the average value of $(B'_1 - B_1)$ is 0.620 T. The uncertainty, 0.024 T, is largely from the spread of the values for the different samples. With $(B_2 - B_1) = 6.52 \pm 0.07$ T, Eq. (7) then gives $Y = 0.1902 \pm 0.0076$. The curve $n=1$ in Fig. 10 then gives $X = J^{(2)}/J^{(1)} = 0.0475 \pm 0.0014$, which leads to $J^{(2)}/k_B = -0.208 \pm 0.006$ K. This result for $J^{(2)}$ is in satisfactory agreement with $J^{(2)}/k_B = -0.227 \pm 0.010$ K from the low-field MSTs due to $J^{(2)}$ pairs. The question if the ratio $J^{(2)}/J_1$ for these materials is sufficiently small for the working model to qualify as “lopsided” is discussed in Appendix B.

The overlap of the two most-intense lines in the field region $n=2$ (Fig. 9) is stronger than the overlap in the region $n=1$ (Fig. 7). As a result, the accuracy for $(B'_2 - B_2)$ is lower than that for $(B'_1 - B_1)$. The experimental values in Table I give the ratio $(B'_2 - B_2)/(B'_1 - B_1) \cong 0.71$. The theoretically predicted ratio, from Fig. 10 and $J^{(2)}/J^{(1)} = 0.047$, is 0.73. The agreement supports the interpretation of these spectral lines.

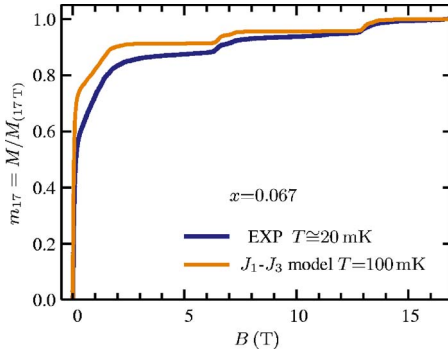


FIG. 11. (Color online) Comparison of the full magnetization curve for $x=0.067$ and a simulation based on the J_1 - J_3 model. The simulation uses the exchange constants $J_1/k_B=J^{(1)}/k_B=-4.39$ K, $J_3/k_B=J^{(2)}/k_B=-0.208$ K, and an effective temperature $T=100$ mK.

3. Undetermined identity of the neighbor associated with $J^{(2)}$

The effort to identify the particular neighbor in the cation lattice that corresponds to $J^{(2)}$ was unsuccessful. As discussed in Refs. 10 and 11, the most likely possibilities are the second and third neighbors. To choose between these alternatives on the basis of MST data alone, the observed MST spectra should be compared with simulations based on the two possibilities. The correct choice of neighbor should lead not only to good agreement, but also to a significantly better agreement than for the alternative choice of neighbor.^{21,22}

Numerical simulations of the magnetization curve are based on the assumption of a random Mn distribution over the cation sites. The validity of this assumption is crucial for identifying the neighbor. Unfortunately, the earlier work⁸ had indicated that at least in some of the samples the Mn distribution was not strictly random. This earlier finding raised the question whether the deviations from a random Mn distribution were large enough to spoil the possibility of identifying the neighbor.

Comparisons of the experimental magnetization curves with simulations were made for the full magnetic-field range (0 to 17 T), and for limited field ranges of special interest, namely, the LF, $n=1$, and $n=2$ field ranges. Nonthermal line broadening was approximated by using an effective temperature of 100 mK in the simulations. (The conclusions do not hinge on this approximation.) The simulations used the exchange constants $J_1/k_B=-4.39$ K and $J^{(2)}/k_B=-0.208$ K, from the high-field data.

For the full field range, both choices $J^{(2)}=J_2$ and $J^{(2)}=J_3$ led only to a qualitative agreement with the simulations. The details were not well reproduced, as illustrated in Fig. 11, which compares the full magnetization curve for $x=0.067$ with a simulation based on the J_1 - J_3 model. The simulation from the J_1 - J_2 model (not shown) is practically indistinguishable on the scale of this figure. For all three samples ($x=0.063$, 0.067, and 0.157) the comparison between the results for the full field range and the simulations did not lead to a clear choice of the neighbor associated with $J^{(2)}$.

The most pronounced differences between simulations based on the J_1 - J_2 and the J_1 - J_3 model are in the field region $n=1$. Figure 12(a) shows the simulations from both models

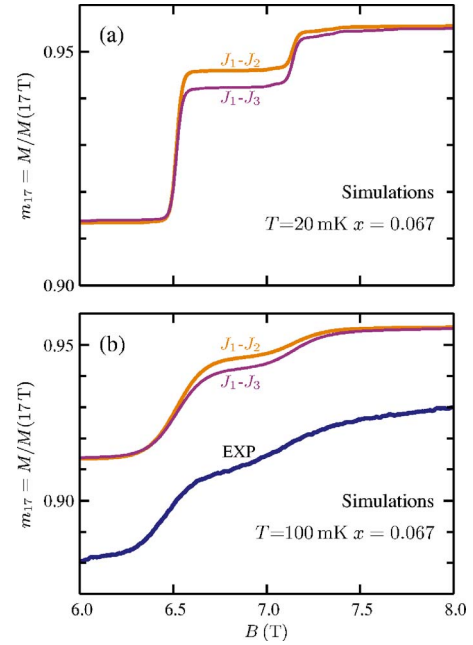


FIG. 12. (Color online) (a) Two simulations of magnetization curve in the field region $n=1$, assuming that $x=0.067$ and $T=20$ mK. One simulation uses the J_1 - J_2 model, and the other the J_1 - J_3 model. The exchange constants are $J_1/k_B=-4.39$ K and $J^{(2)}/k_B=-0.208$ K, where $J^{(2)}$ is either J_2 or J_3 . (b) Comparison of the experimental magnetization curve (EXP) for $x=0.067$ at $T=20$ mK with simulations based on the J_1 - J_2 and J_1 - J_3 models. An effective temperature of 100 mK is used in these simulations.

for $x=0.067$, when $T=20$ mK. Either simulation shows the largest two steps in this field range. The bigger of these two steps, at $B_1 \cong 6.5$ T, is from the pure J_1 pairs. The magnetization jump at this step is called $(\Delta M)_1$. The smaller step, at B'_1 , is from mixed J_1 - $J^{(2)}$ triplets. Its magnitude is called $(\Delta M)'_1$. The sum $(\Delta M)_1 + (\Delta M)'_1$ is nearly the same for both $J^{(2)}=J_2$ and $J^{(2)}=J_3$. However, the ratio $(\Delta M)_1/(\Delta M)'_1$ is smaller for $J^{(2)}=J_3$.

The results in Fig. 12(a) assume a random Mn distribution. The difference between the ratios $(\Delta M)_1/(\Delta M)'_1$ for $J^{(2)}=J_2$ and for $J^{(2)}=J_3$ is not huge, but is adequate for identifying the neighbor experimentally provided that it is known that the Mn distribution is random. Once again the issue is if the deviations from a random distribution are large enough to prevent a reliable determination of the neighbor.

Comparisons of the experimental curve in the region $n=1$ with simulations were carried out for all three samples. Figure 12(b) shows the comparisons for $x=0.067$. Unlike the simulations in Fig. 12(a), the simulations in Fig. 12(b) use an effective temperature $T=100$ mK, to allow for nonthermal broadening.

The experimental ratio $(\Delta M)_1/(\Delta M)'_1$ for $x=0.067$ was estimated from the magnetization curve in Fig. 12(b). An alternative estimate was made by decomposing the derivative curve in Fig. 7 into two peaks and integrating each peak. The estimated experimental ratios $(\Delta M)_1/(\Delta M)'_1$ were then compared with the theoretical values for the alternative choices of the neighbor associated with $J^{(2)}$. The same type of analysis was carried out for the other two samples. Neither choice

of neighbor led to good agreement for all three samples. Therefore, a definite conclusion as to whether $J^{(2)}$ is J_2 or J_3 could not be reached.

V. DISCUSSION

The main result is the measurement of $J^{(2)}$ by two independent methods that use completely different features of the MST spectrum. The magnitude of $J^{(2)}$ is only 5% of $J^{(1)}$. Nevertheless, $J^{(2)}$ was still determined with an accuracy of about 10%.

The present work also verified two important theoretical results for lopsided working models with two exchange constants.¹¹ The predicted low-field MSTs from $J^{(2)}$ pairs were observed. In much higher magnetic fields, the two strongest lines in the FS resulting from the splitting of MST's from $J^{(1)}$ pairs were also observed. The splitting is due to $J^{(2)}$.

Not all the original goals of the present work were achieved. Some were thwarted by less than ideal material properties. The compounds $(\text{CH}_3\text{-NH}_3)_2\text{Mn}_x\text{Cd}_{1-x}\text{Cl}_4$ are among the better physical realizations of a diluted Heisenberg antiferromagnet on the square lattice, but they are not ideal. The known crystallographic phase transitions probably resulted in strains, and possibly also in small (unresolved) line splitting. It is likely that these strains and line splitting led to nonthermal broadening, which degraded the resolution.

A more serious material problem was the Mn distribution. The earlier MST study indicated that this distribution was not quite random. A likely cause was the growth of the materials from solutions, near room temperature.⁸ In most diluted magnetic materials that are grown from the melt at much higher temperatures the distribution of the magnetic ions is random.¹ The nonrandom Mn distributions was probably a major factor in spoiling the identification of the neighbor associated with $J^{(2)}$.

ACKNOWLEDGMENTS

This work was supported by CNPQ and FAPESP. Travel funds for one of the authors (Y.S.) were also provided by FAPESP.

APPENDIX A: MAXIMUM CLUSTER SIZE IN THE WORKING MODEL

1. Choice of maximum cluster size n_{max}

Theoretical calculations of the magnetization curve and of the MST spectrum involve the exact evaluation of the ‘‘truncated sum.’’ This sum contains the contributions of all cluster types of sizes $n_c \leq n_{\text{max}}$ (see Sec. II D). The labor involved in the evaluation of the truncated sum increases rapidly with increasing n_{max} . Therefore, an excessively large n_{max} is impractical.

In the present work the choice of n_{max} was influenced primarily by the labor associated with diagonalizing Hamiltonian matrices for clusters of spins $S=5/2$. The labor of calculating cluster probabilities was not the limiting factor.

The number of Hamiltonian matrices that are diagonalized is equal to the number of cluster types. With increasing n_{max} , not only does this number increase rapidly (see Sec. II B 3), but the matrices become larger. The method which was used was a numerical diagonalization of sparse matrices using MATLAB.²³ The method also took advantage of certain symmetry properties of the Hamiltonian, as described in Ref. 1. The choice $n_{\text{max}}=5$ was based on the labor involved. All cluster types and their probabilities, for cluster sizes up to 5, were given in Ref. 10.

2. Adequacy of the choice $n_{\text{max}}=5$

To assess the accuracy of the MST spectrum calculated with any choice of n_{max} it is useful to note that singles do not produce MSTs. Therefore only clusters with sizes $n_c > 1$ need to be considered. A sufficient condition for the spectrum to be reasonably accurate is that the vast majority of all spins that are in clusters with sizes $n_c > 1$ are actually in cluster with sizes $2 \leq n_c \leq n_{\text{max}}$. If this condition is not met, the calculated spectrum is incomplete.

Because cluster probabilities tend to decrease with cluster size, even when the sufficient condition stated above is not met, the calculated spectrum will include the most pronounced spectral lines. The missing lines will be large in number, but their intensities are expected to be relatively weak. Lines that are missing in the calculation are important only if their intensities are large enough to be detected experimentally.

When the sufficient condition is not met, the magnetization curve calculated from the truncated sum alone is definitely not accurate, even if the missing lines are weak. For the choice $n_{\text{max}}=5$, this shortcoming can be partially remedied if the working model is lopsided. The magnetization from the remainder may then be approximated by the ‘‘corrective quintets method’’ described in Ref. 11.

Let f be the fraction of the total number of nonsingle spins that are actually in clusters of sizes $2 \leq n_c \leq n_{\text{max}}$. This fraction depends on several factors: it increases with n_{max} , it decreases with the Mn concentration x , and it is lower for the $J_1\text{-}J_3$ model than for the $J_1\text{-}J_2$ model because the percolation concentration x_c is lower. The previously stated sufficient condition, which guarantees that the spectrum is reasonably accurate, can be expressed as $(1-f) \leq 1$.

Using the recent results of Bindilatti¹⁵ the fraction f was evaluated for any n_{max} up to 8. The following results are for the Mn concentrations of the samples in the present work when $n_{\text{max}}=5$.

(1) $x=0.063$: $f=0.978$ for the $J_1\text{-}J_2$ model, and 0.956 for the $J_1\text{-}J_3$ model.

(2) $x=0.067$: $f=0.973$ for the $J_1\text{-}J_2$ model, and 0.947 for the $J_1\text{-}J_3$ model.

(3) $x=0.157$: $f=0.702$ for the $J_1\text{-}J_2$ model, and 0.556 for the $J_1\text{-}J_3$ model.

These results indicate that the choice $n_{\text{max}}=5$ is satisfactory for the samples with $x=0.063$ and 0.067. For the sample with $x=0.157$, the spectrum calculated using $n_{\text{max}}=5$ fails to include many spectral lines, and the magnetization calculated from the truncated sum alone is definitely inaccurate.

In Sec. IV E 2 the results for $J^{(2)}$ were based on the splitting between the strongest two lines (2-1 and 3-3 lines) in the field region $n=1$. The consistency of the results for the three samples strongly suggests that (1) these lines were correctly identified in all three samples, including the sample with $x=0.157$, and (2) the many lines from cluster types with $n_c > 5$ did not have any significant affect on the separation between the 2-1 and 3-3 lines for $x=0.157$. Also, in the entire field range that was studied there was no clear evidence in the measured spectrum for any lines from clusters with $n_c > 5$. That is, the lines from these large clusters were sufficiently weak and/or sufficiently broad to avoid detection.

APPENDIX B: IS THE WORKING MODEL FOR THESE MATERIALS LOPSIDED?

The “governing criterion” that a working model based on the J_1 - J_2 cluster model is lopsided was discussed in Sec. II C of Ref. 11. The criterion was expressed as an upper limit for the ratio J_2/J_1 . This upper limit depends on the spin S , and on n_{\max} . Numerical results for the upper limit were given for $S=5/2$ and all values of n_{\max} up to 5. For these combinations of S and n_{\max} (at least) the numerical criteria that a working model based on the J_1 - J_3 model is lopsided are the same, except, of course, that the upper limits are for J_3/J_1 instead of J_2/J_1 .

For the present materials, $S=5/2$. Assuming that $J^{(2)}$ is either J_2 or J_3 , the criterion that a J_1 - $J^{(2)}$ model is lopsided, is $J^{(2)}/J_1 < 0.10$ for both $n_{\max}=2$ and $n_{\max}=3$; $J^{(2)}/J_1 < 0.0450$ for $n_{\max}=4$; and $J^{(2)}/J_1 < 0.0364$ for $n_{\max}=5$. The experimental values of J_1 and $J^{(2)}$ give $J^{(2)}/J_1=0.052$ or 0.047 . Thus, for $n_{\max}=2$ and $n_{\max}=3$ the criterion for a lopsided model is well satisfied. For $n_{\max}=4$ the criterion is not quite satisfied. For the choice $n_{\max}=5$, the criterion for a lopsided model is not satisfied.

Although the working model is not strictly lopsided if $n_{\max}=4$ or 5, the analysis that led to the values of the exchange constants remains completely valid. One reason is that the analysis used only spectral lines from clusters of sizes $n_c=2$ or 3 (pairs and triplets). Therefore, it was only necessary for the model to be lopsided for $n_{\max}=3$.

Another reason is that the analysis did not use all the spectral lines in the full field range up to 17 T. The failure of the working model to be lopsided when n_{\max} is above 3 means only that for these values of n_{\max} there is no gap in the spectrum.¹¹ That is, if spectral lines from clusters up to quartets ($n_{\max}=4$), or up to quintets ($n_{\max}=5$), are included then there is some overlap between the low-field and high-field parts of the spectrum. For the actual ratio $J^{(2)}/J_1$ the magnetic-field range where overlap occurs is relatively narrow: only a portion of the range from 2.5 T to 6.0 T. The spectrum in the overlap region was not used in the analysis that led to the exchange constants.

*Electronic address: vbindilatti@if.usp.br

[†]Electronic address: yshapira@granite.tufts.edu

¹Y. Shapira and V. Bindilatti, *J. Appl. Phys.* **92**, 4155 (2002).

²D. Gatteschi and R. Sessoli, *Magnetic Properties of Large Clusters* (Wiley-VCH, Weinheim, 2002), Chap. 3, pp. 63–108.

³L. J. de Jongh and A. R. Miedema, *Adv. Phys.* **23**, 1 (1974).

⁴*Magnetic Properties of Layered Transition Metal Compounds*, edited by L. J. de Jongh (Kluwer, Dordrecht, 1989).

⁵S. A. Crooker, N. Samarth, and D. D. Awschalom, *Phys. Rev. B* **61**, 1736 (2000).

⁶W. D. van Amstel and L. de Jongh, *Solid State Commun.* **11**, 1423 (1972).

⁷B. Schröder, V. Wagner, N. Lehner, K. M. Kesharwani, and R. Geick, *Phys. Status Solidi B* **97**, 501 (1980).

⁸A. Paduan-Filho, X. Gratens, V. Bindilatti, N. F. Oliveira, Jr., and Y. Shapira, *Phys. Rev. B* **72**, 064415 (2005).

⁹V. Bindilatti and Y. Shapira, *Phys. Rev. B* **72**, 064414 (2005).

¹⁰Y. Shapira and V. Bindilatti, cond-mat/0609701 (unpublished). Various topics in this lengthy work will be discussed in separate future papers.

¹¹Y. Shapira and V. Bindilatti, cond-mat/0609715 (unpublished). Selected topics in this work will be discussed in separate future papers.

¹²K. Malarz and S. Galam, *Phys. Rev. E* **71**, 016125 (2005).

¹³H. P. Peters, D. Stauffer, H. P. Holters, and K. Loewenich, *Z. Phys. B* **34**, 399 (1979).

¹⁴D. Stauffer and A. Aharony, *Introduction to Percolation Theory*, 2nd ed. (Taylor and Francis, London, 1994).

¹⁵V. Bindilatti (unpublished).

¹⁶T. Q. Vu, Ph.D. thesis, Tufts University, 1992.

¹⁷V. Bindilatti, N. F. Oliveira, Jr., E. terHaar, and Y. Shapira, *Czech. J. Phys.* **46**, 3255 (1996).

¹⁸In the model used here, only the largest exchange constant $J^{(1)}=J_1$ and the second-largest exchange constant $J^{(2)}$ are included. A J_1 pair is called “pure” if it is not attached to any $J^{(2)}$ bond.

¹⁹H. B. Boesch and F. Waldner, *Local properties of phase transitions*, edited by K. A. Mýller and A. Rigamonti (North Holland, Amsterdam, 1976), p. 642ff.

²⁰The simulations in Fig. 5 assume a random Mn distribution, and use the J_1 - J_3 model. However, the linewidths do not depend on these assumptions. Results of simulations based on the J_1 - J_2 model are practically the same.

²¹V. Bindilatti, E. ter Haar, N. F. Oliveira, Jr., Y. Shapira, and M. T. Liu, *Phys. Rev. Lett.* **80**, 5425 (1998).

²²X. Gratens, V. Bindilatti, N. F. Oliveira, Jr., Y. Shapira, S. Foner, Z. Golacki, and T. E. Haas, *Phys. Rev. B* **69**, 125209 (2004).

²³The MathWorks, Inc., Natick, MA.